THE JOURNAL OF PHYSICAL CHEMISTRY C

Article

pubs.acs.org/JPCC

Highly Efficient Broad-Band Luminescence Involving Organic and Inorganic Molecules in a Zero-Dimensional Hybrid Lead Chloride

Aymen Yangui,[*,†] Rachel Roccanova,[†] Yuntao Wu,[‡,§,∥] Mao-Hua Du,[⊥] and Bayrammurad Saparov[*,†]

[†]Department of Chemistry and Biochemistry, University of Oklahoma, 101 Stephenson Parkway, Norman, Oklahoma 73019, United States

[‡]Synthetic Crystal Research Center, Shanghai Institute of Ceramics, Chinese Academy of Sciences Shanghai, Shanghai 201800, China

[§]Scintillation Materials Research Center and [∥]Department of Materials Science and Engineering, University of Tennessee, Knoxville, Tennessee 37996, United States

[⊥]Materials Science and Technology Division, Oak Ridge National Laboratory, Oak Ridge, Tennessee 37831, United States

Supporting Information

ABSTRACT: The photophysical mechanism of ultrabright visible light emission in the zero-dimensional (0D) hybrid organic−inorganic material (HOIM), (DETA)$PbCl_5{\cdot}H_2O$ (DETA: diethyltrimonium), has been studied. This compound exhibits efficient room-temperature bluish white light (WL) emission, corroborated by a high photoluminescence quantum yield (PLQY) value of 36.8 % and a Commission Internationale de l'Eclairage (CIE) color coordinates of (0.18, 0.17). Optical investigations reveal that broad-band emission containing multiple emission centers originates from both the fluorescence of the organic molecules DETA and self-trapped excitons within the $[Pb_2Cl_{10}]^{6-}$ inorganic bioctahedra dimers. Furthermore, an enhanced PLQY of up to 40.3% with an adjusted pure WL emission (CIE of (0.33, 0.34)) and a remarkable color rendering index of 90 was achieved through the incorporation of Mn^{2+} within (DETA)$PbCl_5{\cdot}H_2O$. These findings aid in understanding the photophysical properties of 0D HOIMs and preparation of new families of highly emissive materials for solid-state lighting applications.

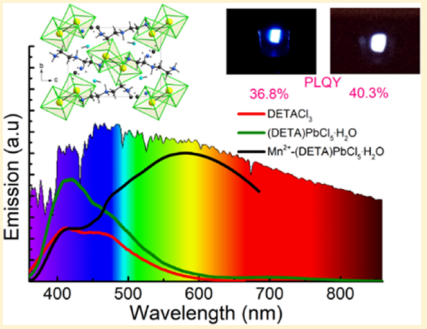

1. INTRODUCTION

Recently, solution-processable hybrid organic−inorganic materials (HOIMs) have attracted considerable attention due to their outstanding photophysical properties, which make them promising candidates for a variety of applications.[1] Among the fascinating properties of these materials is white light (WL) emission, which was first reported in some two-dimensional (2D) HOIMs,[2−4] and attributed to self-trapped excitons (STEs).[2−4] Since then, the number of HOIMs WL emitters have been expanded to include low-dimensional materials, demonstrating unique interesting structural properties and new photophysics including light emission contributions originating from free excitons, structural defects, and bound excitons localized in organic and inorganic moieties.[5−16] It has been evidenced that lowering the structural dimensionality of HOIMs enables strong quantum and dielectric confinement effects. In combination, these effects provide highly localized charges resulting in high exciton binding energies (E_b) and high photoluminescence quantum yield (PLQY).[11,14,17−19] In particular, for single-layered 2D lead halides, broad-band emissions with large Stokes shifts occur as a result of STEs localized on highly distorted inorganic substructures.[6−8] However, this need not be the case, as careful materials design approaches could yield materials in which the organic cations also contribute to the observed broad-band light emission.[11,13,20,21] Building on these ideas, we report a bright bluish WL emission with PLQY of 36.8% involving contribution from both fluorescence of organic molecules DETA and STEs within the $[Pb_2Cl_{10}]^{6-}$ inorganic anions in a new zero-dimensional (0D) HOIM, (DETA)$PbCl_5{\cdot}H_2O$, which advantageously shows high air and thermal stability. Furthermore, by incorporating Mn^{2+} within (DETA)$PbCl_5{\cdot}H_2O$, we could enhance the PLQY to 40.3% and optimize the Commission Internationale de l'Eclairage (CIE) color coordinates to be very close to the pure WL emission. Moreover, the resultant Mn^{2+}@(DETA)$PbCl_5{\cdot}H_2O$ displays a color rendering index (CRI) of 90, a value that meets the requirements for color-critical high-level requirements such as surgery, museum galleries, and cinematography.[18]

2. EXPERIMENTAL SECTION

2.1. Synthesis. All starting reagents were purchased from commercial sources and used without further purification

Received: June 10, 2019
Revised: August 12, 2019
Published: August 13, 2019

ACS Publications © XXXX American Chemical Society

DOI: 10.1021/acs.jpcc.9b05509
J. Phys. Chem. C XXXX, XXX, XXX−XXX

unless otherwise stated. All syntheses steps were conducted in air.

$DETACl_3$ organic salt was prepared using the reaction between stoichiometric amounts of DETA and HCl (37 wt %). The solution was well stirred for 30 min. Then, the solvent was evaporated by heating at 100 °C using a rotary evaporator. Finally, to ensure the product purity, the resulting colorless precipitate was washed with diethylether and dried under vacuum.

Single crystals of $(DETA)PbCl_5{\cdot}H_2O$ were obtained by slow solvent evaporation at room temperature. Stoichiometric amounts of $PbCl_2$ were added to the precursor $DETACl_3$ salt, stirred well in 2 mL of dimethyl sulfoxide solvent, and kept at room temperature. After 1 day, centimeter scale colorless platelets were formed.

A $MnCl_2/(DETA)PbCl_5{\cdot}H_2O$ = 5:100 molar ratio mixture was prepared by mixing the freshly prepared single crystals of $(DETA)PbCl_5{\cdot}H_2O$ with $MnCl_2$. The mixture was thoroughly ground for 10 min, then added to a glass vial and annealed at 80 °C in an oven for 90 min. Finally, the sample was allowed to cool to room temperature and was used further for characterization. It is worth noting that our attempts to grow single crystals of Mn^{2+}@$(DETA)PbCl_5{\cdot}H_2O$ using the solvent evaporation technique described above for $(DETA)PbCl_5{\cdot}H_2O$ were unsuccessful.

2.2. Single-Crystal X-ray Diffraction. Single-crystal X-ray diffraction (SXRD) data were collected on a Bruker D8 Quest with a Kappa geometry goniometer, an Incoatec Imus X-ray source (graphite monochromated Mo Kα (λ = 0.71073 Å) radiation), and a Photon II detector. The data were corrected for absorption using the semiempirical method based on equivalent reflections, and the structures were solved by intrinsic phasing methods (SHELXT) as embedded in the APEX3 v2016.9.0 program.[22] All atoms except hydrogens were refined with anisotropic displacement parameters. Site occupancy factors were checked by freeing occupancies of each unique crystallographic site. Details of the data collection and crystallographic parameters are given in Table 1. Atomic coordinates, equivalent isotropic displacement parameters, and selected interatomic distances and bond angles are provided in Tables 1 and S1 in the Supporting Information (SI). Additional information on the crystal structures investigations can be obtained in the form of a crystallographic information file (CIF), which was deposited in the Cambridge Crystallographic Data Denter (CCDC) database (deposition numbers 1903945 for $(DETA)PbCl_5{\cdot}H_2O$ and 1911266 for $DETACl_3$).

2.3. Powder X-ray Diffraction. Powder X-ray diffraction (PXRD) measurements were carried out at room temperature on a Rigaku MiniFlex600 system equipped with a D/tex detector using a Ni-filtered Cu Kα radiation source. Typical PXRD scans were collected in the 3−90° (2θ) range, with a step size of 0.02°. The collected room-temperature PXRD data of $(DETA)PbCl_5{\cdot}H_2O$ were fitted using the crystal structure obtained from SXRD 100 K via the decomposition method (also known as Pawley fitting) as embedded in Rigaku's PDXL2 software package.[23] To study the air stability of $(DETA)PbCl_5{\cdot}H_2O$, a finely ground polycrystalline powder sample was left in ambient air on a laboratory bench for 3 months. During this period, PXRD patterns were measured periodically under the same measurement conditions as described above.

2.4. Thermal Stability Analysis. Simultaneous thermogravimetric analysis (TGA) and differential scanning calorimetry (DSC) measurements were carried out on a TA Instruments SDT650 unit. Measurements were done in 90 μL alumina crucibles on 5 mg samples under a 100 mL min^{-1} flow of nitrogen in the 45−500 °C range with 5 °C min^{-1} heating rate. TGA results suggest no mass loss up to ∼200 °C (SI, Figure S1). Moreover, DSC scan suggests that $(DETA)PbCl_5{\cdot}H_2O$ undergo two distinct endothermic temperature events at T_1 = 220 °C and T_2 = 305 °C (Figure S1), attributed to the melting of the material[24] and, subsequently, complete evaporation of the compound above 300°C. The observed thermal behavior of $(DETA)PbCl_5{\cdot}H_2O$ is comparable to that of other HOIMs reported in the literature.[15,25,26]

Table 1. Selected Single-Crystal Data and Structure Refinement Parameters for $(DETA)PbCl_5{\cdot}H_2O$ and $DETACl_3$[b]

formula	$(C_4H_{16}N_3)PbCl_5{\cdot}H_2O$	$C_4H_{14}N_3Cl_3$
formula weight (g mol^{-1})	339.10	212.55
temperature (K)	100(2)	
radiation, wavelength (Å)	Mo Kα, 0.71073	
crystal system	monoclinic	orthorhombic
space group	$P2_1/c$	$Pmmn$
Z	6	2
unit cell parameters (Å)	a = 10.1570(2)	a = 5.0798(3)
	b = 10.2787(2)	b = 21.2450(12)
	c = 14.5711(3)	c = 4.7211(3)
	ß = 109.6914(6)°	
volume (Å^3)	1432.28(5)	509.50(5)
density (ρ_{calc}) (g cm^{-3})	2.359	1.385
absorption coefficient (μ) (mm^{-1})	12.690	0.843
θ_{min} − θ_{max} (deg)	2.13−31.00	3.836−28.288
reflections collected	31 566	4300
independent reflections	4548	718
R[a] indices ($I > 2\sigma(I)$)	R_1 = 1.68	R_1 = 3.63
	wR_2 = 3.93	wR_2 = 9.95
goodness-of-fit on F^2	1.228	1.002
largest diff. peak and hole (e^- Å^{-3})	0.916 and −1.455	0.384 and −0.410

[a] $R_1 = \sum||F_0| - |F_c||/\sum|F_0|$; w$R_2 = |\sum|w(F_0^2 - F_c^2)/\sum|wF_0^{22}|^{1/2}$ [b] where $w = 1/|\sigma^2F_0^2 + (AP)^2 + BP|$, with $P = (F_0^2 + 2F_c^2)/3$ and weight coefficients A and B.

2.5. Optical Measurements. Room-temperature diffuse reflectance spectra of polycrystalline powder of $(DETA)PbCl_5{\cdot}H_2O$ and $DETACl_3$ were measured using a high-resolution PerkinElmer LAMBDA 750 UV−vis−NIR spectrometer equipped with a 100 mm InGaAs integrating sphere attachment.

Excitation-dependent photoluminescence (PL), photoluminescence excitation (PLE), and PLQY measurements were performed at ambient temperature on polycrystalline powder samples, using a HORIBA Jobin Yvon Fluorolog-3 spectrofluorometer using a Xenon lamp and Quanta-φ integrating sphere. PLQY data were analyzed using the two-curve method in a varied range from 280 to 800 nm. Care was taken to avoid any appearance of interference from primary and secondary overtones from the source lamp as the measurements were taken. Moreover, to ensure the reliability of PLQYs measurements, the integrated sphere was calibrated by using sodium salicylate as standard sample (PLQY = 56%).[27] The measurements performed on different samples yield PLQY value variations up to ∼3%.

DOI: 10.1021/acs.jpcc.9b05509
J. Phys. Chem. C XXXX, XXX, XXX−XXX

Time-resolved photoluminescence (TRPL) measurements were done on single-crystal samples using a HORIBA Jobin Yvon Fluorolog-3 spectrofluorometer equipped with time-correlated single photon counting module. HORIBA Jobin Yvon NanoLEDs (pulsed light-emitting diodes) were used as the excitation source. The duration of the light pulse was shorter than 2 ns. Temperature- and power-dependent PL spectra were measured on single-crystal sample using a double monochromator U1000 equipped with a photomultiplier. The excitation wavelength was the 325 nm (3.815 eV) line of a Spectra Physics Beamlock 2085 argon laser. The sample was placed in a helium bath cryostat, and the measurements were performed between 4 and 295 K.

The CIE chromaticity diagram values were calculated using OSRAM Company's ColorCalculator software available from https://www.osram-americas.com.

Raman spectra of (DETA)$PbCl_5$·H_2O were recorded on a Renishaw InVia Reflex Raman Mapping Microscope. The excitation line was 633 nm. The laser beam was focused onto the sample through a Leica-X50 microscope objective, and the laser spot dimension was ~10 μm^2 and the excitation power was 10 mW.

2.6. First-Principles Calculations. All calculations were based on density functional theory (DFT) implemented in the VASP code.[28] The interaction between ions and electrons was described by the projector augmented wave method.[29] The kinetic energy cutoff of 400 eV was used for the plane-wave basis. Experimental lattice parameters were used while the atomic positions were fully relaxed until the residual forces were less than 0.02 eV $Å^{-1}$. Electronic band structure and density of states (DOS) of (DETA)$PbCl_5$·H_2O were calculated using the Perdew−Burke−Ernzerhof (PBE) exchange-correlation functional,[30] while the exciton properties were treated by using more advanced hybrid PBE0 functional,[31] which has 25% nonlocal Fock exchange. A PBE calculation usually underestimates band gap, while hybrid functional calculations significantly improve the band gap description by partially correcting the self-interaction error.[31−33] The partial correction of the self-interaction error also leads to better description of charge localization and stability of hole/electron polarons and STEs.[34−38] The total energy of an exciton was calculated by fixing the occupation numbers of the electron and hole-occupied eigenlevels [Δ self-consistent field (ΔSCF) method[39−41]]. The ΔSCF method can be easily used in (DETA)$PbCl_5$·H_2O because the electron and hole are both localized on a single Pb_2Cl_{10} cluster and each occupies one single eigenlevel deep inside the band gap.[42] Such localized electron and hole levels are found for both unrelaxed and relaxed excitons. The ΔSCF method combined with the hybrid PBE0 functional allows excited-state structural relaxation and has shown accurate results in exciton excitation and emission energies in many compounds.[17,38,42−48] Following the Franck−Condon principle, the exciton excitation and emission energies were obtained by calculating the total energy differences between the excited and ground states using PBE0-optimized ground-state and excited-state structures, respectively.

3. RESULTS AND DISCUSSION

(DETA)$PbCl_5$·H_2O crystallizes in the monoclinic space group $P2_1/c$ featuring edge-sharing bioctahedral $[Pb_2Cl_{10}]^{6-}$ units surrounded by bulky organic $[DETA]^{3+}$ cations (Figure 1).

Based on room-temperature PXRD measurements on polycrystalline powder of (DETA)$PbCl_5$·H_2O (Figure 2a), a phase-pure sample was obtained using wet methods. The room-temperature PXRD pattern of (DETA)$PbCl_5$·H_2O can be well refined using our SXRD results obtained at 100 K, ruling out the possibility of the presence of structural phase transitions between 100 K and room temperature, often observed in several HOIMs.[5,49−51] Moreover, polycrystalline powder of (DETA)$PbCl_5$·H_2O shows good ambient air stability for more than 3 months (Figure 2b) and thermal stability up to ~200 °C, comparable to that of other HOIMs reported in the literature (Figure S1).[15,25] On the other hand, the purity of the organic salt $DETACl_3$ was also confirmed through room-temperature PXRD measurements, which shows a good agreement with the simulated pattern obtained from SXRD (Figure 2c).

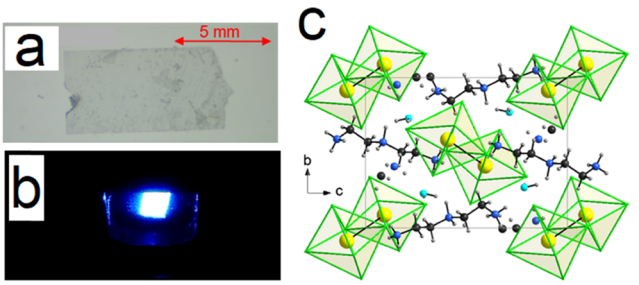

Figure 1. Optical microscopy images of as-prepared single crystal of (DETA)$PbCl_5$·H_2O under (a) ambient light and (b) 325 nm UV irradiation, showing the bright bluish WL emission at room temperature. (c) Projection of crystal structure of (DETA)$PbCl_5$·H_2O along the crystallographic *a*-axis. Yellow, pink, blue, black, blue, turquoise, and gray spheres represent Pb, Cl, C, N, O, and H atoms, respectively. The edge-sharing $[Pb_2Cl_{10}]^{6-}$ bioctahedra are emphasized in green.

As shown in Figure 1b, a bright bluish WL emission with the corresponding CIE color coordinates of (0.18, 0.17) is observed at ambient temperature upon UV irradiation. To probe the origin of this bright emission, we carried out comprehensive studies of optical properties (DETA)$PbCl_5$·H_2O and the corresponding organic salt $DETACl_3$. The optical absorption spectrum of (DETA)$PbCl_5$·H_2O shows two absorption bands at 4.19 and 4.54 eV accompanied with a shoulder at 3.62 eV. The absorption band of 3.62 eV is corroborated by the presence of a sharp PLE peak at 3.62 eV (Figure 3a), and therefore, is assigned to the electronic transition from the top of the valence band (VB) including Pb(6s) and Cl(3p) orbitals to Pb(6p) orbital at the bottom of the conduction band (CB),[13,52] within the inorganic bioctahedra Pb_2Cl_{10}.[13,52] On the other hand, the 4.19 and 4.54 eV absorption features of (DETA)$PbCl_5$·H_2O are attributed to the organic $DETACl_3$ absorption (Figure 3a). Upon 3.815 eV irradiation, the room-temperature PL spectrum of (DETA)$PbCl_5$·H_2O shows a high-efficiency broad-band bluish WL emission clearly observed even by the naked eye (Figure 1b). This includes multiple emission peaks with main maxima at 2.99 eV (P4), two shoulders at 2.70 (P3) and 2.58 eV (P2), and a low-energy broad band at 1.78 eV (P1) (Figure 2a). Moreover, by using a higher excitation energy of 4.2 eV, we could also detect the inorganic exciton emission at 3.54 eV (noted Pex in Figure S2a), usually observed in PbCl-based HOIMs,[13,52] which suggest that the band gap of (DETA)$PbCl_5$·H_2O is higher than 3.82eV. The emission spectrum of the organic salt $DETACl_3$ was also measured under identical conditions (Figure 3a). Results show that $DETACl_3$ itself

DOI: 10.1021/acs.jpcc.9b05509
J. Phys. Chem. C XXXX, XXX, XXX−XXX

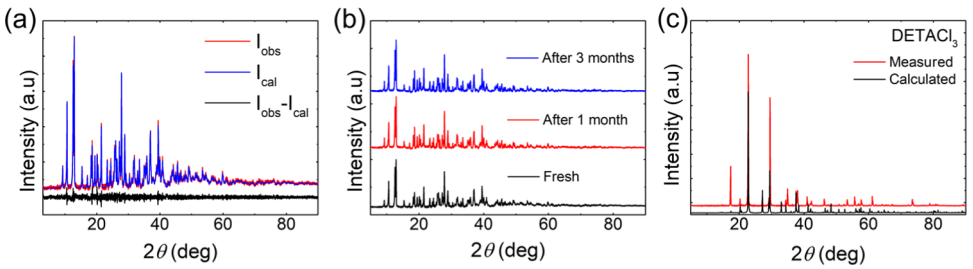

Figure 2. (a) Powder XRD patterns (red) of (DETA)$PbCl_5 \cdot H_2O$. Pawley fits and difference plots are shown in blue and black, respectively. (b) PXRD patterns of (DETA)$PbCl_5 \cdot H_2O$ left in ambient air and measured periodically for over a period of 3 months. (c) Measured (red) and calculated (black) PXRD patterns of the ammonium salt $DETACl_3$, at room temperature.

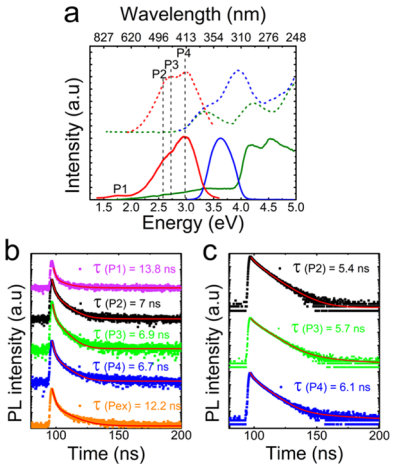

Figure 3. (a) Room-temperature absorbance (green lines), PLE (blue lines, E_{em} = 2.99), and PL spectra (red lines, E_{ex} = 3.815 eV) of $DETACl_3$ (doted lines) and (DETA)$PbCl_5 \cdot H_2O$ (solid lines). The dashed black lines show that P2−P4 PL peaks of (DETA)$PbCl_5 \cdot H_2O$ result from $DETACl_3$ organic salts emission. Room-temperature time-resolved PL spectra of (b) (DETA)$PbCl_5 \cdot H_2O$ and (c) $DETACl_3$ measured under 4.2 eV excitation energy.

exhibits a broad-band emission formed by three sub-bands almost at the same position as P2−P4 in (DETA)$PbCl_5 \cdot H_2O$. Furthermore, we observed a good agreement between the high energy emission of $DETACl_3$ and (DETA)$PbCl_5 \cdot H_2O$ and found that the shape of the emission spectra of the organic salt $DETACl_3$ is nearly independent of the excitation energy (Figure S2b). Moreover, the measurement of the room-temperature emission spectrum of as-purchased DETA (liquid, >99% purity) furthermore shows the presence of P2−P4 peaks (see Figure S3), which suggests that the P2−P4 emission peaks of $DETACl_3$ and (DETA)$PbCl_5 \cdot H_2O$ refer to DETA molecular fluorescence.[53] Thus, PLE spectrum of $DETACl_3$ measured at an emission energy of 2.99 eV shows a maximum at 3.95 eV accompanied with a shoulder at 3.35 eV due to the excitons in organic molecules, whereas for (DETA)$PbCl_5 \cdot H_2O$, a single broad PLE peak is observed at 3.62 eV, which is attributed to an overlap between the organic and inorganic excitonic absorptions.

Importantly, the measured room-temperature PLQY value of 36.8% for (DETA)$PbCl_5 \cdot H_2O$ is more than an order of magnitude higher than that measured on the organic salt $DETACl_3$ (2.87%), and to the best of our knowledge, represents the highest WL PLQY reported in a 0D lead halide to date.[7,12,14,15] The origin of the PLQY enhancement can be related to greater isolation of molecular organic and inorganic units in 0D hybrid halide structures compared to the parent binary halides and organic salts.

Figure 3b,c shows the TRPL measurements of (DETA)-$PbCl_5 \cdot H_2O$ and $DETACl_3$. All decay profiles can be fitted using the biexponential function[54]

$$I(t) = A_1 \exp\left(-\frac{t}{\tau_1}\right) + A_2 \exp\left(-\frac{t}{\tau_2}\right) \quad (1)$$

where τ_1 and τ_2 are the PL lifetime, and A_1 and A_2 are the coefficients of the exponential decay terms. The full refinement results (see Table S2 in the SI) show that the fastest fitting component, τ_2, is dominant for all emission peaks and measure τ_2 (P1) = 13.8 ns, τ_2 (P2) = 7 ns, τ_2 (P3) = 6.9 ns, τ_2 (P4) = 6.7 ns, and τ_2 (Pex) = 12.2 ns for (DETA)$PbCl_5 \cdot H_2O$, and τ_2 (P2) = 5.4 ns, τ_2 (P3) = 5.7 ns, and τ_2 (P4) = 6.1 ns for $DETACl_3$. These fast decay times (5−7 ns) support the assignment of P2−P4 peaks to the emission of DETA molecules as the observed fluorescence from singlet excitons in organic molecules is typically fast.[55] However, the low-energy P1 peak, attributed to the emission of STEs localized at $[Pb_2Cl_{10}]^{6-}$ inorganic bioctahedra, shows a slightly larger lifetime of 13.8 ns. The delay in the STE formation is based on the consideration of an energy barrier that is required to be surmounted.[56] This fact could explain the longer relaxation time for low-energy P1 peak compared to the organic P2−P4 fluorescence bands. Note that the presence of permanent defect states can also promote a broad-band emission. However, the concentration and recombination lifetime of permanent defects are finite, and therefore, their emission intensities should saturate at higher excitation power.[57] Here, as shown in Figure 4, the evolution of the intensity of P1 as a function of excitation power demonstrates a linear behavior, which excludes the possibility of permanent defect emission.[4,6,12]

To get further information about the thermally activated processes, we measured the temperature-dependent PL of (DETA)$PbCl_5 \cdot H_2O$ under 3.815 eV excitation (Figure 5a). The thermal quenching of the emission is relatively insignificant confirming the high thermal stability of excitons (PL 4/300 K ∼ 2), which further supports the high measured PLQY value of 36.8% at room temperature. Based on the fitting of temperature-dependent PL data (Figure S4), we studied the thermal evolution of the integrated intensity, position, and full width at half-maximum (FWHM) of emission peaks (Figures 5b−d and S5). The P2−P4 PL peak positions are almost temperature-independent, whereas the low-energy P1 peak first blue-shifts up to 150 K and then red-shifts as temperature is further increased. The markedly different behavior of P1 compared to P2−P4 peaks is

DOI: 10.1021/acs.jpcc.9b05509
J. Phys. Chem. C XXXX, XXX, XXX−XXX

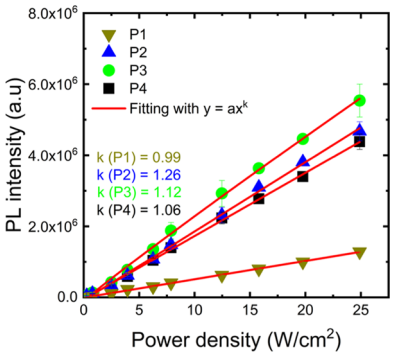

Figure 4. Power-dependent PL spectra of $(DETA)PbCl_5 \cdot H_2O$ measured at 4 K and upon 3.815 eV excitation. The red lines show the fitting used $y = ax^k$.

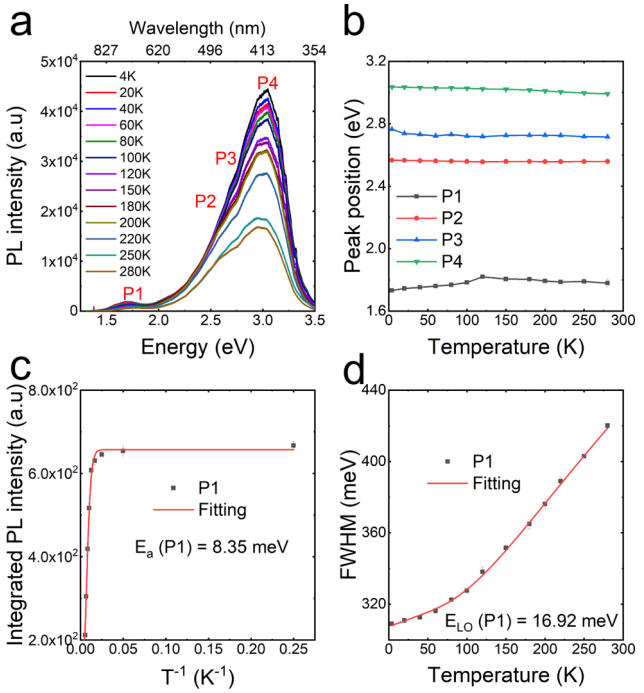

Figure 5. (a) Temperature-dependent PL spectra of $(DETA)PbCl_5 \cdot H_2O$ upon 3.815 eV irradiation. (b–d) Thermal evolution of position, integrated intensity, and FWHM of PL peaks.

indicative of a different emission mechanism, supporting our earlier assignments. Moreover, by fitting the thermal quenching of the integrated intensities of P1 peak using an Arrhenius-type model,[58] we estimated an activation energy of E_a (P1) = 10.21 meV, which is comparable to those previously reported values[4,15,59] and corresponds to the Raman vibration mode of 82 cm^{-1} (Figure S6) of $(DETA)PbCl_5 \cdot H_2O$, which is well within the range of Pb–Cl stretching frequencies.[13,59] Furthermore, the thermal broadening in FWHM of the P1 PL peak could be described by[60]

$$\Gamma(T) = \Gamma_0 + \Gamma_{AC} \times T + \Gamma_{LO} \times (1 + \exp(E_{LO}/k_B T)^{-1} \quad (2)$$

where the first term is the natural line width at 0 K, the second term represents the broadening induced by acoustic phonons, and the third term corresponds to the contribution of optical phonons to the peak broadening. Here, Γ_{LO} is the exciton–phonon coupling constant and E_{LO} is the optical phonon energy. The best-fitting parameters yield Γ_{LO} = 385 meV K^{-1} and E_{LO} = 16.9 meV. The high exciton–phonon coupling constant value of 385 meV K^{-1} is 1 order of magnitude larger than those of lead-based three-dimensional hybrid perovskites (Γ_{LO} of 40–61 meV),[61] suggesting a greatly increased strength of the electron–phonon coupling in $(DETA)PbCl_5 \cdot H_2O$.[62] Moreover, the E_{LO} value of 16.9 meV is in excellent agreement with the Raman mode of 137 cm^{-1} (Figure S6). These findings support the assignment of the low-energy P1 PL peak to phonon-assisted radiative recombination of STEs.

To further understand the electronic structure and exciton properties of $(DETA)PbCl_5 \cdot H_2O$, we performed first-principles calculations. The calculated band structure shows flat CB and VB (Figure 6a) indicating the localized nature of these

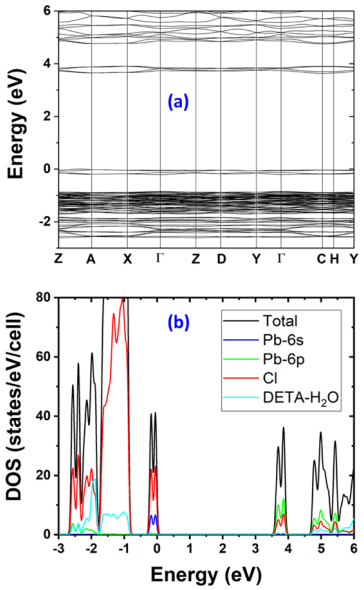

Figure 6. Electronic band structure and density of states (DOS) plots for $(DETA)PbCl_5 \cdot H_2O$, calculated using the PBE functional. Note that the band gap is underestimated due to the well-known band gap error of the PBE calculation.

bands consistent with the 0D structure. The CB and VB are primarily distributed on Pb_2Cl_{10} clusters as can be seen from the density of states (DOS) plot (Figure 6b). The VB is made up of Pb 6s and Cl 3p orbitals, while the CB is derived from Pb 6p and Cl 3p orbitals. The calculated excitons are localized at a single Pb_2Cl_{10} cluster (Figure 7). Two different types of excitons (EX-1 and EX-2) were found in calculations. The hole and the electron in EX-1 are centered at the same Pb ion, while those in EX-2 are separated on two adjacent Pb ions (Figure 7). EX-2 is more stable than EX-1 by 0.43 eV. The separation of the electron from the hole in an exciton has also been found in other low-dimensional metal halides.[45] This is related to the ability of Pb^{2+} (which has a 6s lone pair) to attract a hole. When the hole is centered at a Pb ion, it attracts the adjacent Cl ions, shortening the Pb–Cl bonds for stronger Coulomb binding. When the electron and the hole are separated in EX-2, the hole center shortens six Pb–Cl bonds. On the other hand, only four Pb–Cl bonds (which are roughly perpendicular to the other two Pb–Cl bonds in the octahedron) are shortened in EX-1. The calculated excitation energy of an exciton is 4.22 eV, and the emission energies of EX-1 and EX-2 are 3.55 and 1.85 eV, respectively, which present an excellent agreement

DOI: 10.1021/acs.jpcc.9b05509
J. Phys. Chem. C XXXX, XXX, XXX–XXX

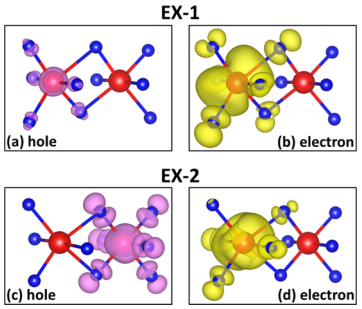

Figure 7. Isosurfaces of the partial charge density (0.0005 e bohr^{-3}) of hole and electron in two different excitons [EX-1 (a, b) and EX-2 (c, d)] in (DETA)$PbCl_5{\cdot}H_2O$, calculated using the hybrid PBE0 functional. The hole and electron are centered at the same Pb ion in EX-1 but distributed on two adjacent Pb ions in EX-2. Pb and Cl ions are represented by red and blue balls, respectively.

with the measured Pex and P1 emission peaks of (DETA)-$PbCl_5{\cdot}H_2O$ (Pex for Ex-1 and P1 for Ex-2).

In combination, highly efficient emission from molecular organic and inorganic units in (DETA)$PbCl_5{\cdot}H_2O$ provides a broad bluish emission spectrum; however, blue emission dominates, and as mentioned above, the measured CIE coordinates of (0.18, 0.17) indicate that the emission color is far from the white point of (0.33, 0.33). To optimize the WL emission properties of (DETA)$PbCl_5{\cdot}H_2O$, a strategy can be adopted according to which emission from another component, either dopants or impurities, helps red-shift the maximum of the broad-band emission.

As a preliminary demonstration of the validity of this approach, we prepared a powder sample of Mn^{2+}@(DETA)-$PbCl_5{\cdot}H_2O$, in which a small amount (5%) of $MnCl_2$, a known source of red-emitting Mn^{2+}, is incorporated into (DETA)-$PbCl_5{\cdot}H_2O$ (details in the SI file). As shown in Figure 8, the PXRD pattern of Mn^{2+}@(DETA)$PbCl_5{\cdot}H_2O$ demonstrates that the peak positions systematically shift toward higher angles (by 0.2°), confirming the successful incorporation of

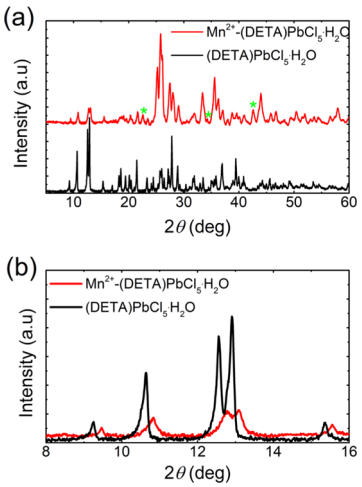

Figure 8. (a) PXRD pattern of Mn^{2+}-incorporated host (DETA)-$PbCl_5{\cdot}H_2O$ and (b) a magnified view of 8−16° showing the shift of the PXRD peak positions. A systematical shift of peaks positions toward higher angles by 0.2°, which confirms the successful incorporation of Mn^{2+} into the host crystal lattice sites of (DETA)$PbCl_5{\cdot}H_2O$. Impurities peaks are indicated with green asterisks in (a).

Mn^{2+} into the host crystal lattice sites. Although this process is yet to be optimized, importantly, the room-temperature PL measurement of Mn^{2+}@(DETA)$PbCl_5{\cdot}H_2O$ (Figure 9)

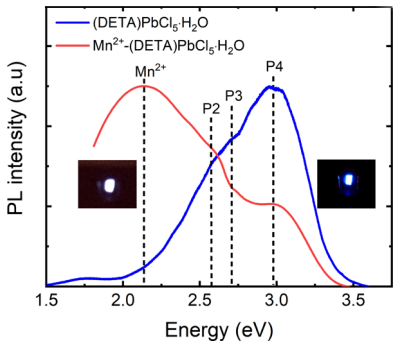

Figure 9. Room-temperature PL spectra of (blue, E_{ex} = 3.815 eV) (DETA)$PbBr_5{\cdot}H_2O$ and (red, E_{ex} = 3.54 eV) Mn^{2+}-doped (DETA)-$PbBr_5{\cdot}H_2O$.

confirms the successful red-shifting of the emission spectrum. Note that the P2−P4 emission peaks of (DETA)$PbCl_5{\cdot}H_2O$ are preserved upon Mn^{2+} incorporation and the emergence of the new low-energy 2.14 eV peak is due to $4T_1 \rightarrow 6A_1$ Mn^{2+} electronic transition.[63−66] In combination with emissions from the organic and inorganic molecular ions, emission from Mn^{2+} centers provides a pure WL emission with CIE coordinates of (0.33, 0.34), yielding a very high CRI of 90 (see Figure S7) among the highest values reported in the literature to date.[19,21] Furthermore, a notable enhancement of the PLQY value from 36.8 to 40.3% occurs due to the efficient exciton trapping by defects created by Mn^{2+} dopants, which is consistent with the recent findings on other related Mn^{2+}-incorporated lead halide perovskites.[65−67]

4. CONCLUSIONS

In summary, we report the synthesis, crystal structure, and optical properties of the new 0D HOIM, (DETA)$PbCl_5{\cdot}H_2O$, which shows a remarkably efficient bluish WL emission at room temperature with a PLQY of 36.8%, which is among the highest reported for the lead-based halides. The origin of this broad and bright visible emission is determined to be from an overlapping fluorescence of the organic molecules DETA and STE within the $[Pb_2Cl_{10}]^{6-}$ inorganic bioctahedra. We also demonstrate that the WL properties of the title compound could be optimized through the incorporation of small amounts (5%) of Mn^{2+} source additive leading to PLQY enhancement and an adjusted pure WL emission (CIE of (0.33, 0.34)) as well as a remarkable color rendering index of 90. This work demonstrates that by understanding the origin of luminescence in HOIMs, a molecular-level materials design approach can be developed in which the light emission properties of a given material selectively originate from organic molecules, inorganic substructures, or dopants/impurities.

■ ASSOCIATED CONTENT

Supporting Information

The Supporting Information is available free of charge on the ACS Publications website at DOI: 10.1021/acs.jpcc.9b05509.

TGA/DSC, excitation dependence PL, CIE diagram, and Raman spectroscopy measurements; CCDC

DOI: 10.1021/acs.jpcc.9b05509
J. Phys. Chem. C XXXX, XXX, XXX−XXX

1903945 and 1911266 contains the supplementary crystallographic data (CIFs) (PDF)

AUTHOR INFORMATION

Corresponding Authors

*E-mail: aymen.yangui@ou.edu.

*E-mail: saparov@ou.edu.

ORCID

Aymen Yangui: 0000-0002-6695-972X

Mao-Hua Du: 0000-0001-8796-167X

Author Contributions

The manuscript was written through the contributions of all authors. All authors have given approval to the final version of the manuscript. A.Y. prepared the sample, did the measurements, and wrote the paper. R.R. assisted on SXRD measurements. Y.W. did the time-resolved photoluminescence measurements, M.-H.D. did the DFT calculations, and B.S. supervised the work.

Notes

The authors declare no competing financial interest.

ACKNOWLEDGMENTS

This work was supported by the University of Oklahoma startup funds. M.-H.D. was supported by the U.S. Department of Energy, Office of Science, Basic Energy Sciences, Materials Sciences and Engineering Division. The authors acknowledge Dr. Douglas R. Powell for technical assistance with the single-crystal X-ray diffraction measurements (supported by NSF grant CHE-1726630).

REFERENCES

(1) Kovalenko, M. V.; Protesescu, L.; Bodnarchuk, M. I. Properties and Potential Optoelectronic Applications of Lead Halide Perovskite Nanocrystals. *Science* **2017**, *358*, 745−750.

(2) Dohner, E. R.; Hoke, E. T.; Karunadasa, H. I. Self-Assembly of Broadband White-Light Emitters. *J. Am. Chem. Soc.* **2014**, *136*, 1718−1721.

(3) Dohner, E. R.; Jaffe, A.; Bradshaw, L. R.; Karunadasa, H. I. Intrinsic White-Light Emission from Layered Hybrid Perovskites. *J. Am. Chem. Soc.* **2014**, *136*, 13154−13157.

(4) Yangui, A.; Garrot, D.; Lauret, J. S.; Lusson, A.; Bouchez, G.; Deleporte, E.; Pillet, S.; Bendeif, E. E.; Castro, M.; Triki, S.; et al. Optical Investigation of Broadband White-Light Emission in Self-Assembled Organic-Inorganic Perovskite $(C_6H_{11}NH_3)_2PbBr_4$. *J. Phys. Chem. C* **2015**, *119*, 23638−23647.

(5) Yangui, A.; Pillet, S.; Mlayah, A.; Lusson, A.; Bouchez, G.; Triki, S.; Abid, Y.; Boukheddaden, K. Structural Phase Transition Causing Anomalous Photoluminescence Behavior in Perovskite $(C_6H_{11}NH_3)_2[PbI_4]$. *J. Chem. Phys.* **2015**, *143*, No. 224201.

(6) Hu, T.; Smith, M. D.; Dohner, E. R.; Sher, M.-J.; Wu, X.; Trinh, M. T.; Fisher, A.; Corbett, J.; Zhu, X. Y.; Karunadasa, H. I.; et al. Mechanism for Broadband White-Light Emission from Two-Dimensional (110) Hybrid Perovskites. *J. Phys. Chem. Lett.* **2016**, *7*, 2258−2263.

(7) Smith, M. D.; Jaffe, A.; Dohner, E. R.; Lindenberg, A. M.; Karunadasa, H. I. Structural Origins of Broadband Emission from Layered Pb−Br Hybrid Perovskites. *Chem. Sci.* **2017**, *8*, 4497−4504.

(8) Yangui, A.; Pillet, S.; Lusson, A.; Bendeif, E. E.; Triki, S.; Abid, Y.; Boukheddaden, K. Control of the White-Light Emission in the Mixed Two-Dimensional Hybrid Perovskites $(C_6H_{11}NH_3)_2[PbBr_{4-x}I_x]$. *J. Alloys Compd.* **2017**, *699*, 1122−1133.

(9) Yangui, A.; Pillet, S.; Bendeif, E.-E.; Lusson, A.; Triki, S.; Abid, Y.; Boukheddaden, K. Broadband Emission in a New Two-Dimensional Cd-Based Hybrid Perovskite. *ACS Photonics* **2018**, *5*, 1599−1611.

(10) Brochard-Garnier, S.; Paris, M.; Génois, R.; Han, Q.; Liu, Y.; Massuyeau, F.; Gautier, R. Screening Approach for the Discovery of New Hybrid Perovskites with Efficient Photoemission. *Adv. Funct. Mater.* **2019**, *29*, No. 1806728.

(11) Roccanova, R.; Houck, M.; Yangui, A.; Han, D.; Shi, H.; Wu, Y.; Glatzhofer, D. T.; Powell, D. R.; Chen, S.; Fourati, H.; et al. Broadband Emission in Hybrid Organic−Inorganic Halides of Group 12 Metals. *ACS Omega* **2018**, *3*, 18791−18802.

(12) Smith, M. D.; Karunadasa, H. I. White-Light Emission from Layered Halide Perovskites. *Acc. Chem. Res.* **2018**, *51*, 619−627.

(13) Barkaoui, H.; Abid, H.; Yangui, A.; Triki, S.; Boukheddaden, K.; Abid, Y. Yellowish White-Light Emission Involving Resonant Energy Transfer in a New One-Dimensional Hybrid Material: $(C_9H_{10}N_2)$-$PbCl_4$. *J. Phys. Chem. C* **2018**, *122*, 24253−24261.

(14) Zhou, J.; Li, M.; Ning, L.; Zhang, R.; Molokeev, M. S.; Zhao, J.; Yang, S.; Han, K.; Xia, Z. Broad-Band Emission in a Zero-Dimensional Hybrid Organic $[PbBr_6]$ Trimer with Intrinsic Vacancies. *J. Phys. Chem. Lett.* **2019**, *10*, 1337−1341.

(15) Gautier, R.; Massuyeau, F.; Galnon, G.; Paris, M. Lead Halide Post-Perovskite-Type Chains for High-Efficiency White-Light Emission. *Adv. Mater.* **2019**, *31*, No. 1807383.

(16) Sharma, M.; Yangui, A.; Whiteside, V. R.; Sellers, I. R.; Han, D.; Chen, S.; Du, M.-H.; Saparov, B. $Rb_4Ag_2BiBr_9$: A Lead-Free Visible Light Absorbing Halide Semiconductor with Improved Stability. *Inorg. Chem.* **2019**, *58*, 4446−4455.

(17) Roccanova, R.; Yangui, A.; Nhalil, H.; Shi, H.; Du, M.-H.; Saparov, B. Near-Unity Photoluminescence Quantum Yield in Blue-Emitting $Cs_3Cu_2Br_{5-x}I_x$ $(0 \le x \le 5)$. *ACS Appl. Electron. Mater.* **2019**, *1*, 269−274.

(18) Rea, M. S.; Freyssinier, J. P. Color Rendering: Beyond Pride and Prejudice. *Color Res. Appl.* **2010**, *35*, 401−409.

(19) Wang, G.-E.; Xu, G.; Wang, M.-S.; Cai, L.-Z.; Li, W.-H.; Guo, G.-C. Semiconductive 3-D Haloplumbate Framework Hybrids with High Color Rendering Index White-Light Emission. *Chem. Sci.* **2015**, *6*, 7222−7226.

(20) Krishnamurthy, S.; Naphade, R.; Mir, W. J.; Gosavi, S.; Chakraborty, S.; Vaidhyanathan, R.; Ogale, S. Molecular and Self-Trapped Excitonic Contributions to the Broadband Luminescence in Diamine-Based Low-Dimensional Hybrid Perovskite Systems. *Adv. Opt. Mater.* **2018**, *6*, No. 1800751.

(21) Yangui, A.; Roccanova, R.; McWhorter, T. M.; Wu, Y.; Du, M.-H.; Saparov, B. Hybrid Organic-Inorganic Halides $(C_5H_7N_2)_2MBr_4$ (M = Hg, Zn) with High Color Rendering Index and High-Efficiency White-Light Emission. *Chem. Mater.* **2019**, *31*, 2983−2991.

(22) Sheldrick, G. A short history of SHELX. *Acta Crystallogr., A* **2008**, *64*, 112−122.

(23) *PDXL2*.Rigaku Corporation: Tokyo, Japan, 2012.

(24) Mann, F. G. Hofmann's Ethylene Bases. Synthesis of *ββ′*-Diaminodiethylamine and of *ββ′*-Diaminodiethylmethylamine. *J. Chem. Soc.* **1934**, 461−466.

(25) Liu, X.; Huang, T. J.; Zhang, L.; Tang, B.; Zhang, N.; Shi, D.; Gong, H. Highly Stable, New, Organic-Inorganic Perovskite $(CH_3NH_3)_2PdBr_4$: Synthesis, Structure, and Physical Properties. *Chem. - Eur. J.* **2018**, *24*, 4991−4998.

(26) Dang, Y.; Liu, Y.; Sun, Y.; Yuan, D.; Liu, X.; Lu, W.; Liu, G.; Xia, H.; Tao, X. Bulk Crystal Growth of Hybrid Perovskite Material $CH_3NH_3PbI_3$. *CrystEngComm* **2015**, *17*, 665−670.

(27) Bai, X.; Caputo, G.; Hao, Z.; Freitas, V. T.; Zhang, J.; Longo, R. L.; Malta, O. L.; Ferreira, R. A. S.; Pinna, N. Efficient and Tuneable Photoluminescent Boehmite Hybrid Nanoplates Lacking Metal Activator Centres for Single-phase White LEDs. *Nat. Commun.* **2014**, *5*, No. 5702.

(28) Kresse, G.; Furthmüller, J. Efficiency of Ab-initio Total Energy Calculations for Metals and Semiconductors Using a Plane-wave Basis Set. *Comput. Mater. Sci.* **1996**, *6*, 15−50.

(29) Kresse, G.; Joubert, D. From Ultrasoft Pseudopotentials to the Projector Augmented-wave Method. *Phys. Rev. B* **1999**, *59*, No. 1758.

DOI: 10.1021/acs.jpcc.9b05509
J. Phys. Chem. C XXXX, XXX, XXX−XXX

(30) Perdew, J. P.; Burke, K.; Ernzerhof, M. Generalized Gradient Approximation Made Simple. *Phys. Rev. Lett.* **1996**, *77*, No. 3865.
(31) Perdew, J. P.; Emzerhof, M.; Burke, K. Rationale for Mixing Exact Exchange with Density Functional Approximations. *J. Chem. Phys.* **1996**, *105*, 9982−9985.
(32) Heyd, J.; Scuseria, G. E.; Ernzerhof, M. Hybrid Functionals Based on a Screened Coulomb Potential. *J. Chem. Phys.* **2003**, *118*, 8207−8215.
(33) Paier, J.; Marsman, M.; Hummer, K.; Kresse, G.; Gerber, I. C.; Angyan, J. G. Screened Hybrid Density Functionals Applied to Solids. *J. Chem. Phys.* **2006**, *124*, No. 154709.
(34) Du, M.-H.; Zhang, S. B. Impurity-bound Small Polarons in ZnO: Hybrid Density Functional Calculations. *Phys. Rev. B* **2009**, *80*, No. 115217.
(35) Janotti, A.; Varley, J. B.; Choi, M.; Van de Walle, C. G. Vacancies and Small Polarons in $SrTiO_3$. *Phys. Rev. B* **2014**, *90*, No. 085202.
(36) Janotti, A.; Franchini, C.; Varley, J. B.; Kresse, G.; Van de Walle, C. G. Dual Behavior of Excess Electrons in Rutile TiO_2. *Phys. Status Solidi RRL* **2013**, *7*, 199−203.
(37) Bjaalie, L.; Ouellette, D. G.; Moetakef, P.; Cain, T. A.; Janotti, A.; Himmetoglu, B.; Allen, S. J.; Stemmer, S.; Walle, C. G. V. D. Small Hole Polarons in Rare-earth Titanates. *Appl. Phys. Lett.* **2015**, *106*, No. 232103.
(38) Biswas, K.; Du, M. H. Energy Transport and Scintillation of Cerium-doped Elpasolite Cs_2LiYCl_6: Hybrid Density Functional Calculations. *Phys. Rev. B* **2012**, *86*, No. 014102.
(39) Jones, R. O.; Gunnarsson, O. The Density Functional Formalism, Its Applications and Prospects. *Rev. Mod. Phys.* **1989**, *61*, 689−746.
(40) Görling, A. Density-functional Theory Beyond the Hohenberg-Kohn Theorem. *Phys. Rev. A* **1999**, *59*, 3359−3374.
(41) Hellman, A.; Razaznejad, B.; Lundqvist, B. I. Potential-energy Surfaces for Excited States in Extended Systems. *J. Chem. Phys.* **2004**, *120*, 4593−4602.
(42) Han, D.; Shi, H.; Ming, W.; Zhou, C.; Ma, B.; Saparov, B.; Ma, Y.-Z.; Chen, S.; Du, M.-H. Unraveling Luminescence Mechanisms in Zero-dimensional Halide Perovskites. *J. Mater. Chem. C* **2018**, *6*, 6398−6405.
(43) Zhou, C.; Lin, H.; Shi, H.; Tian, Y.; Pak, C.; Shatruk, M.; Zhou, Y.; Djurovich, P.; Du, M.-H.; Ma, B. A Zero-Dimensional Organic Seesaw-Shaped Tin Bromide with Highly Efficient Strongly Stokes-Shifted Deep-Red Emission. *Angew. Chem., Int. Ed.* **2018**, *57*, 1021.
(44) Zhou, C.; Worku, M.; Neu, J.; Lin, H.; Tian, Y.; Lee, S.; Zhou, Y.; Han, D.; Chen, S.; Hao, A.; et al. Facile Preparation of Light Emitting Organic Metal Halide Crystals with Near-Unity Quantum Efficiency. *Chem. Mater.* **2018**, *30*, 2374−2378.
(45) Wu, G.; Zhou, C.; Ming, W.; Han, D.; Chen, S.; Yang, D.; Besara, T.; Neu, J.; Siegrist, T.; Du, M.-H.; et al. A One-Dimensional Organic Lead Chloride Hybrid with Excitation-Dependent Broadband Emissions. *ACS Energy Lett.* **2018**, *3*, 1443−1449.
(46) Zhou, C.; Lin, H.; He, Q.; Xu, L.; Worku, M.; Chaaban, M.; Lee, S.; Shi, X.; Du, M.-H.; Ma, B. Low Dimensional Metal Halide Perovskites and Hybrids. *Mater. Sci. Eng., R* **2019**, *137*, 38−65.
(47) Wang, X.; Meng, W.; Liao, W.; Wang, J.; Xiong, R.-G.; Yan, Y. Atomistic Mechanism of Broadband Emission in Metal Halide Perovskites. *J. Phys. Chem. Lett.* **2019**, *10*, 501−506.
(48) Du, M.-H. Zero-dimensional Metal Oxide $Li4TiO_4$. *J. Mater. Chem. C* **2019**, *7*, 5710−5715.
(49) Yangui, A.; Sy, M.; Li, L.; Abid, Y.; Naumov, P.; Boukheddaden, K. Rapid and Robust Spatiotemporal Dynamics of the First-order Phase Transition in Crystals of the Organic-Inorganic Perovskite $(C_{12}H_{25}NH_3)_2PbI_4$. *Sci. Rep.* **2015**, *5*, No. 16634.
(50) Dobrovolsky, A.; Merdasa, A.; Unger, E. L.; Yartsev, A.; Scheblykin, I. G. Defect-induced Local Variation of Crystal Phase Transition Temperature in Metal-Halide Perovskites. *Nat. Commun.* **2017**, *8*, No. 34.
(51) Yangui, A.; Pillet, S.; Garrot, D.; Triki, S.; Abid, Y.; Boukheddaden, K. Evidence and Detailed Study of a Second-Order Phase Transition in the $(C_6H_{11}NH_3)_2[PbI_4]$ Organic-Inorganic Hybrid Material. *J. Appl. Phys.* **2015**, *117*, No. 115503, 1-9 .
(52) Li, Y.; Lin, C.; Zheng, G.; Lin, J. Synthesis, Structure and Optical Properties of New Organic−Inorganic Haloplumbates Complexes $(C_5H_{10}N_3)PbX_4$ (X= Br, Cl), $(C_2H_2N_4)PbBr_3$. *J. Solid State Chem.* **2007**, *180*, 173−179.
(53) Fang, H.; Jena, P. Molecular Origin of Properties of Organic-Inorganic Hybrid Perovskites: The Big Picture from Small Clusters. *J. Phys. Chem. Lett.* **2016**, *7*, 1596−1603.
(54) Baloch, A. A. B.; Alharbi, F. H.; Grancini, G.; Hossain, M. I.; Nazeeruddin, M. K.; Tabet, N. Analysis of Photocarrier Dynamics at Interfaces in Perovskite Solar Cells by Time-Resolved Photo-luminescence. *J. Phys. Chem. C* **2018**, *122*, 26805−26815.
(55) Salas Redondo, C.; Kleine, P.; Roszeitis, K.; Achenbach, T.; Kroll, M.; Thomschke, M.; Reineke, S. Interplay of Fluorescence and Phosphorescence in Organic Biluminescent Emitters. *J. Phys. Chem. C* **2017**, *121*, 14946−14953.
(56) Mott, N. F.; Stoneham, A. M. The Lifetime of Electrons, Holes and Excitons Before Self-Trapping. *J. Phys. C: Solid State Phys.* **1977**, *10*, 3391−3398.
(57) Reshchikov, M. A.; Morkoç, H. Luminescence Properties of Defects in GaN. *J. Appl. Phys.* **2005**, *97*, No. 061301.
(58) Jiang, D.-S.; Jung, H.; Ploog, K. Temperature Dependence of Photoluminescence from GaAs Single and Multiple Quantum-well Heterostructures Grown by Molecular-Beam Epitaxy. *J. Appl. Phys.* **1988**, *64*, 1371−1377.
(59) Thirumal, K.; Chong, W. K.; Xie, W.; Ganguly, R.; Muduli, S. K.; Sherburne, M.; Asta, M.; Mhaisalkar, S.; Sum, T. C.; Soo, H. S.; et al. Morphology-Independent Stable White-Light Emission from Self-Assembled Two-Dimensional Perovskites Driven by Strong Exciton−Phonon Coupling to the Organic Framework. *Chem. Mater.* **2017**, *29*, 3947−3953.
(60) Rudin, S.; Reinecke, T. L.; Segall, B. Temperature-Dependent Exciton Linewidths in Semiconductors. *Phys. Rev. B* **1990**, *42*, 11218−11231.
(61) Wright, A. D.; Verdi, C.; Milot, R. L.; Eperon, G. E.; Pérez-Osorio, M. A.; Snaith, H. J.; Giustino, F.; Johnston, M. B.; Herz, L. M. Electron−Phonon Coupling in Hybrid Lead Halide Perovskites. *Nat. Commun.* **2016**, *7*, No. 11755.
(62) Viswanath, A. K.; Lee, J. I.; Kim, D.; Lee, C. R.; Leem, J. Y. Exciton-Phonon Interactions, Exciton Binding Energy, and Their Importance in the Realization of Room-Temperature Semiconductor Lasers Based on GaN. *Phys. Rev. B* **1998**, *58*, 16333−16339.
(63) Biswas, A.; Bakthavatsalam, R.; Kundu, J. Efficient Exciton to Dopant Energy Transfer in Mn2+-Doped $(C_4H_9NH_3)_2PbBr_4$ Two-Dimensional (2D) Layered Perovskites. *Chem. Mater.* **2017**, *29*, 7816−7825.
(64) Bakthavatsalam, R.; Biswas, A.; Chakali, M.; Bangal, P. R.; Kore, B. P.; Kundu, J. Temperature-Dependent Photoluminescence and Energy-Transfer Dynamics in Mn^{2+}-Doped $(C_4H_9NH_3)_2PbBr_4$ Two-Dimensional (2D) Layered Perovskite. *J. Phys. Chem. C* **2019**, *123*, 4739−4748.
(65) Sheikh, T.; Nag, A. Mn Doping in Centimeter-Sized Layered 2D Butylammonium Lead Bromide (BA_2PbBr_4) Single Crystals and Their Optical Properties. *J. Phys. Chem. C* **2019**, *123*, 9420−9427.
(66) Usman, M. H. P.; Bakthavatsalam, R.; Kundu, J. Colloidal Mn^{2+} Doped 2D (n =1) Lead Bromide Perovskites: Efficient Energy Transfer and Role of Anion in Doping Mechanism. *ChemistrySelect* **2018**, *3*, 6585−6595.
(67) Gangishetty, M. K.; Sanders, S. N.; Congreve, D. N. Mn2+ Doping Enhances the Brightness, Efficiency, and Stability of Bulk Perovskite Light-Emitting Diodes. *ACS Photonics* **2019**, *6*, 1111−1117.

DOI: 10.1021/acs.jpcc.9b05509
J. Phys. Chem. C XXXX, XXX, XXX−XXX